

Phonon transport in freestanding SrTiO_3 down to the monolayer limit

Qi Wang^{1,*} Chen Wang^{2,*} Cheng Chi³, Niuchang Ouyang², Ruiqiang Guo^{1,†} Nuo Yang^{4,‡} and Yue Chen^{2,§}

¹ Thermal Science Research Center, Shandong Institute of Advanced Technology, Jinan, Shandong Province 250103, China

² Department of Mechanical Engineering, The University of Hong Kong, Pokfulam Road, Hong Kong SAR, China

³ Key Laboratory of Power Station Energy Transfer Conversion and System of Ministry of Education, School of Energy Power and Mechanical Engineering, North China Electric Power University, Beijing 102206, China

⁴ State Key Laboratory of Coal Combustion, School of Energy and Power Engineering, Huazhong University of Science and Technology, Wuhan 430074, China

(Dated: September 14, 2023)

Perovskites down to the monolayer limit have emerged and have attracted increased interest due to their two-dimensional nature with potentially novel physical properties. Here, we investigate the phonon transport in the oxide perovskite SrTiO_3 with thicknesses from the monolayer limit to 10 nm by constructing an accurate first-principles machine learning potential and combining it with the Boltzmann transport equation and homogeneous nonequilibrium molecular dynamics simulations. Compared to its bulk counterpart, the phonon dispersion relation of monolayer SrTiO_3 is insensitive to temperature, and the calculated in-plane thermal conductivity of monolayer SrTiO_3 is much larger than that of bulk SrTiO_3 , which mainly results from the unique out-of-plane atomic vibrations in monolayer SrTiO_3 . The thermal conductivity of SrTiO_3 thin film first decreases and then approaches the bulk value as thickness increases from the monolayer limit to 10 nm. The hardening of the out-of-plane acoustic phonon branch and the transition of low-frequency optical phonons can explain the observed trend in thermal conductivity transitions. Our study demonstrates that monolayer SrTiO_3 has higher thermal conductivity than its bulk counterpart with covalent bonds at the first-principles level of accuracy, and dimension reduction has a weak inhibition on phonon transport in free-standing atomically smooth SrTiO_3 thin films, which further the understanding of phonon transport in two-dimensional perovskite thin films.

I. INTRODUCTION

Perovskites have demonstrated remarkable potential in various applications such as photovoltaic [1, 2], ferroelectric [3], and energy conversion/storage applications [4, 5]. Recently, two-dimensional (2D) perovskites have emerged for their tunable structures [6] and physical properties such as carrier mobility [7], band gap [8, 9], and dielectric constant [10]. For example, the free-standing oxide perovskite SrTiO_3 thin films with different thicknesses, especially the one down to the monolayer limit, have been synthesized [11]. Unlike traditional 2D materials, e.g., graphene and silicene, whose bulk and multi-layer counterparts are stacked by van der Waals interaction, the bulk and thin-film counterparts of monolayer SrTiO_3 share covalent bonds across the thickness direction, which may lead to the discovery of novel physical properties in 2D SrTiO_3 thin films. Recent studies have demonstrated that ultrahigh-dielectric-constant single-crystalline SrTiO_3 ultrathin films, with their elastic and 2D nature, can be used to fabricate short-channel transistors with promising performance [10].

When utilizing the emerging 2D perovskites including 2D SrTiO_3 thin films in various electronic devices, their

thermal properties are the key factor in architecture design for thermal management. However, due to phase transitions and strong anharmonicity of SrTiO_3 and other perovskites, accurately describing phonon transport in perovskites is nontrivial [12, 13]. Recently, phonon properties of bulk SrTiO_3 have been investigated with first-principles-based calculations. Using density functional theory (DFT) or DFT-based machine learning potential method, the anharmonic phonon properties and thermal conductivity of bulk SrTiO_3 have been examined [13–15] through the temperature-dependent effective potential (TDEP) method [16, 17] or the self-consistent phonon (SCPH) theory [18], and the calculated thermal conductivity is in good agreement with experimental measurement [13, 15]. Anharmonic phonon renormalization, temperature-dependent interatomic force constants (IFCs), and four-phonon scattering are regarded as important factors in accurately describing phonon transport properties in bulk SrTiO_3 . The phonon thermal Hall effect [19], electron-phonon interactions [20], and phonon hydrodynamics [21] of bulk SrTiO_3 were also extensively investigated. However, the in-plane phonon transport properties and thermal conductivity of 2D SrTiO_3 thin films with different thicknesses remain unexplored. The effects of phonon renormalization and high-order phonon scattering on phonon transport are obscure for 2D SrTiO_3 thin films. As the thickness of perovskite thin films used in electronic devices is now down to sub-10 nm, heat dissipation becomes an inevitable issue, and a deeper understanding of the size-thermal-conductivity relationship is necessary.

* These authors contributed equally to this work

† ruiqiang.guo@iat.cn

‡ nuo@hust.edu.cn

§ yuechen@hku.hk

Capturing thickness-dependent thermal properties of semiconductors in nanoscale regime is always fundamental yet essential for their applications in electronic devices. For example, the in-plane thermal conductivity of Si thin films with different thicknesses was thoroughly studied via theoretical calculations [22–24] and experimental measurements [25, 26]. Compared to the bulk, largely suppressed in-plane phonon transport in ultrathin Si films is revealed. Thickness-dependent in-plane thermal transport in many 2D materials and their multi-layer van der Waals materials [27, 28] were also investigated to achieve tunable thermal properties. As for 2D SrTiO₃ thin films with increased thickness, the calculation of in-plane thermal conductivity through direct implementation of first-principles methods presents a formidable challenge. Machine learning potentials (MLPs) that merge the accuracy of first-principles calculations with the efficiency of empirical potentials are favorable candidates for enabling accurate atomic simulations of phonon transport of complex systems [29–32]. MLPs have achieved great success in studying phonon transport in various systems [33, 34]. However, using molecular dynamics (MD) simulations to extract the thermal conductivity of SrTiO₃ thin films with up to 10 nm thickness requires a long simulation time, which is still a challenge even for MLPs. Fan *et al.* developed an MLP called neuroevolution potential (NEP) [35, 36] and implemented it in the graphics processing units (GPU) to speed up MD simulations, which can achieve the first-principles accuracy and significantly improve computational efficiency. Here, by constructing an accurate NEP for SrTiO₃ thin films and using the Boltzmann transport equation (BTE) and/or the homogeneous nonequilibrium molecular dynamics (HNEMD) simulations [37], we demonstrate that phonon dispersion of monolayer SrTiO₃ is insensitive to temperature and the in-plane thermal conductivity is much larger than that of bulk SrTiO₃. Our detailed analysis reveals that the pure out-of-plane atomic vibrations in monolayer SrTiO₃ and the consequent quadratic phonon dispersion relation near the Γ point induce an enhanced contribution of low-frequency phonons to thermal conductivity. We also extract the thickness-dependent in-plane thermal conductivity of SrTiO₃ thin films with thickness up to 10 nm and identify that the change of the out-of-plane acoustic (ZA) and low-frequency optical phonon branches with thickness causes the observed trend in thermal conductivity transitions.

II. METHOD

We develop an accurate NEP for free-standing SrTiO₃ thin films using multiple representative configurations based on first-principles calculations. The Projector augmented wave (PAW) method [38] and PBEsol exchange-correlation functional [39] were chosen for DFT optimizations and calculations. The energy cutoff was set to 550

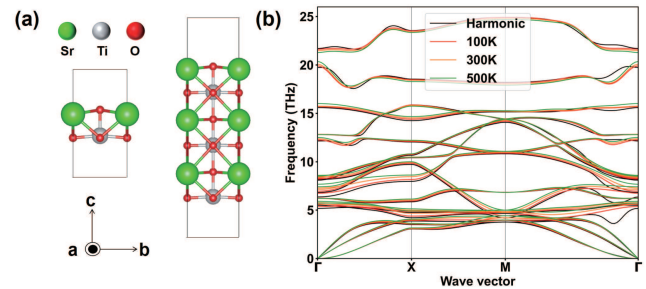


FIG. 1. (a) Crystal structures of SrTiO₃ monolayer (left) and thin film with a thickness of 1.4 nm (right); (b) Harmonic and renormalized phonon dispersions at different temperatures.

eV, and the energy and atomic force convergence criteria were set to 10^{-8} eV and 10^{-6} eV/Å, respectively. The training data set was prepared following an active learning strategy [40, 41]. First, *ab initio* MD (AIMD) simulations [42] with a time step of 2 fs and 500 steps were performed for supercells of cubic SrTiO₃ and free-standing thin films with thicknesses of 5.97, 10.02, and 13.94 Å at 300, 500, and 700 K. Only the Γ point was used for the k -point integration in AIMD simulations. The initial training set was selected to include configurations every ten steps. Then, classical MD simulations using the LAMMPS package [43] with the pre-trained potential and a total of 1 ns for the active learning process were conducted for all systems and temperatures. Finally, 1705 configurations were selected for accurate DFT calculations with a $3 \times 3 \times 3$ ($3 \times 3 \times 1$) k -point mesh for the bulk (thin film) SrTiO₃ to obtain the energies, atomic forces, and virials. In addition, 189 configurations including 50 configurations of the 2.2-nm-thick thin film not in the training set were selected from SrTiO₃ MD trajectories to form the cross-validation set.

The final 1705 configurations with their energies, atomic forces, and virials were used to train an accurate NEP. The hyperparameter values used in the GPUMD package for the training are listed in Table 1. Compared to the DFT calculations, the obtained NEP for SrTiO₃ predicts consistent energies, atomic forces, and virials for the training and cross-validation configurations, as shown in Figs. S1 and S2. For the training set, the root mean square errors (RMSEs) of energies, forces, and virials are 0.60 meV/atom, 59.0 meV/Å, and 7.89 meV/atom, respectively. For the validation set, the RMSEs of energies, forces, and virials are 0.81 meV/atom, 68.7 meV/Å, and 6.87 meV/atom, respectively. To further confirm the ability of the constructed NEP model in predicting phonon properties, harmonic phonon dispersion relations of SrTiO₃ with thicknesses of 5.97, 10.02, and 13.94 Å were calculated using the finite displacement method with DFT and NEP model and compared in Fig. S3. The lattice thermal conductivities of the monolayer and 1.0-nm-thick SrTiO₃ thin film calculated from the DFT and NEP are listed in Table S1. Good agreements are achieved between the NEP and DFT results, demon-

TABLE I. Hyperparameters for the NEP model.

parameter	value	parameter	value
r_c^R	8	r_c^A	5
n_{max}^R	12	n_{max}^A	8
N_{bas}^R	12	n_{bas}^A	8
l_{max}^{3b}	4	l_{max}^{4b}	2
N_{neu}	50	λ_1	0.05
λ_2	0.05	λ_e	1
λ_f	1	λ_v	0.1
N_{bat}	428	N_{pop}	50
N_{gen}	4×10^5		

strating the capacity of the NEP for phonon calculations of SrTiO_3 thin films.

With the NEP, the renormalized phonon dispersions of the monolayer and SrTiO_3 thin films were calculated using the TDEP method. The nonanalytic correction to the dynamic matrix was considered within the PHONOPY package [44]. We adopted both the BTE method as implemented in ShengBTE [45] and FourPhonon [46] packages and the HNEMD simulations as implemented in the GPUMD package to calculate the lattice thermal conductivity of monolayer SrTiO_3 . In the BTE method, phonon anharmonicity up to four-phonon scattering was included, and in the HNEMD method, a small driving force applied to each atom was carefully tested (see the Supplemental Material [47]) and chosen as $1.0 \times 10^{-4} \text{ \AA}^{-1}$. HNEMD simulations were also used to calculate lattice thermal conductivities of SrTiO_3 thin films with different thicknesses. The thickness of a thin film is defined as the summation of the largest vertical distance between two surface atoms and their van der Waals radii, which is consistent with the thickness definition for other 2D materials [48]. The largest thickness in our simulations is 10 nm. More calculation details are included in the Supplemental Material.

III. PHONON TRANSPORT IN MONOLAYER STRONTIUM TITANATE

Bulk SrTiO_3 exhibits a cubic crystal structure above 105 K, and the harmonic phonon dispersion of the cubic phase shows imaginary frequency [13, 18]. Its renormalized phonon dispersion shows obvious temperature dependence as revealed in our previous work [13]. For monolayer SrTiO_3 [the crystal structure is shown in Fig. 1(a)], its harmonic phonon dispersion calculated with the finite displacement method and the renormalized phonon dispersions at different temperatures calculated with the TDEP method are displayed in Fig. 1(b). The renormalized phonon dispersion of the monolayer at different temperatures resembles the harmonic one and demonstrates a weak temperature dependence. It is noticed that the octahedron consisting of one Ti atom and its six adjacent O atoms in bulk SrTiO_3 is broken in monolayer SrTiO_3 , possibly leading to the modified atomic vibra-

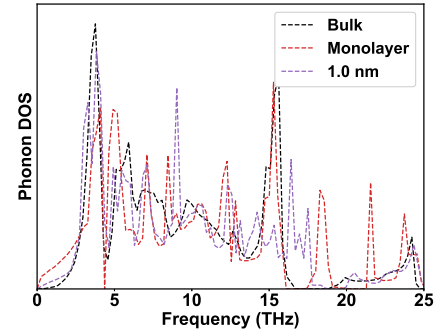


FIG. 2. Phonon DOS of monolayer, bulk, and SrTiO_3 thin film with 1.0 nm thickness at 300 K.

tional modes and affecting the lattice anharmonicity of monolayer SrTiO_3 . We also display the temperature-dependent 3rd and 4th IFCs values in Fig. S5, and only a small difference is observed among IFCs at different temperatures. The weak temperature dependence of renormalized phonon dispersions and high-order IFCs of monolayer SrTiO_3 is distinct from its bulk counterpart. In bulk SrTiO_3 , lattice anharmonicity is related to the tilting and rotation of octahedrons, while in monolayer SrTiO_3 , the octahedral atomic vibrations are missing. In addition, the ZA phonon branch of monolayer SrTiO_3 near the Γ point shows a strictly quadratic dispersion similar to those of other 2D materials [49, 50], while the TA phonon branch of bulk SrTiO_3 is linear. The phonon density of states (DOS) of monolayer SrTiO_3 at low frequency also shows a much larger portion than bulk SrTiO_3 (see Fig. 2), demonstrating the influence of quadratic dispersion of the ZA phonon branch on phonon properties. In contrast, the DOS of a 1.0-nm-thick SrTiO_3 thin film at low frequency shows a small difference compared to the bulk value.

With the NEP, we first determined the thermal conductivity of bulk SrTiO_3 at 300 K under the BTE scheme to be 9.2 W/mK, close to the HNEMD value of 8.5 W/mK, and both results are also in good agreement with previous calculations [13–15] and measurements [15, 51]. Using the temperature-dependent 2nd, 3rd, and 4th IFCs and the BTE method, we calculated the in-plane thermal conductivity of monolayer SrTiO_3 from 100 to 700 K, as plotted in Fig. 3. The HNEMD results are also displayed for comparison. Four-phonon scattering shows a weak influence on the thermal conductivity of monolayer SrTiO_3 at 300 K (only 5.5% reduction) compared to the bulk [13]. The thermal conductivities from both methods at different temperatures show good consistency. The thermal conductivity of monolayer SrTiO_3 is higher than that of bulk SrTiO_3 at 300 K (BTE: 13.9 vs 9.2; HNEMD: 10.5 vs 8.5; unit: W/mK), different from the expectation that classical size effect suppresses phonon transport in covalent solids [22, 52]. In Fig. 4, we plot the cumulative thermal conductivity of both bulk and monolayer SrTiO_3 . For monolayer SrTiO_3 , phonon modes

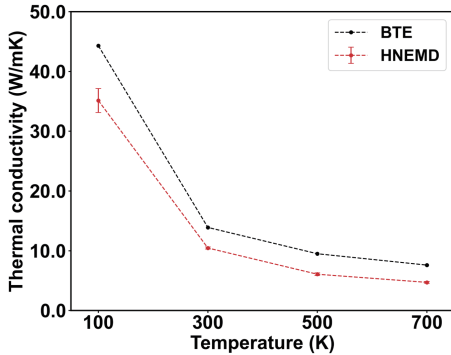


FIG. 3. In-plane thermal conductivity of monolayer SrTiO_3 from 100 to 700 K.

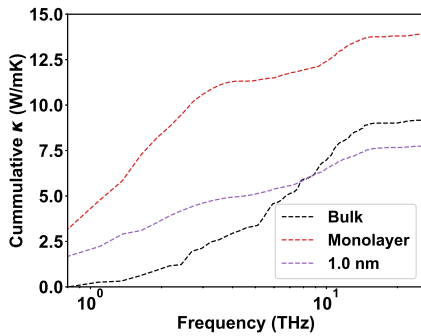


FIG. 4. In-plane cumulative thermal conductivity of the bulk, monolayer, and SrTiO_3 thin film with 1.0 nm thickness.

below 1.8 THz contribute 50% to the thermal conductivity, while for bulk SrTiO_3 , these phonon modes only contribute 15%, which implies the importance of low-frequency (long wavelength) ZA phonon modes in the phonon transport of monolayer SrTiO_3 . The transition of low-frequency acoustic phonon dispersion from bulk to monolayer SrTiO_3 alters both phonon properties and phonon scattering processes, leading to enhanced phonon conduction in monolayer SrTiO_3 . Interestingly, the relation of thermal conductivity between bulk and monolayer SrTiO_3 resembles that between van der Waals materials and their 2D counterparts. For instance, the thermal conductivity of graphene is much higher than that of graphite [27, 53].

IV. IN-PLANE PHONON TRANSPORT IN FREE-STANDING STRONTIUM TITANATE THIN FILMS

For thicker films, the harmonic phonon dispersions show distinct imaginary frequency modes (see Fig. S3). In Fig. 5, using the TDEP method, we calculated the renormalized phonon dispersions of monolayer SrTiO_3 and thin films with thicknesses of 1.0, 1.4, and 3.6 nm at 300 K (the acoustic and the lowest optical phonon

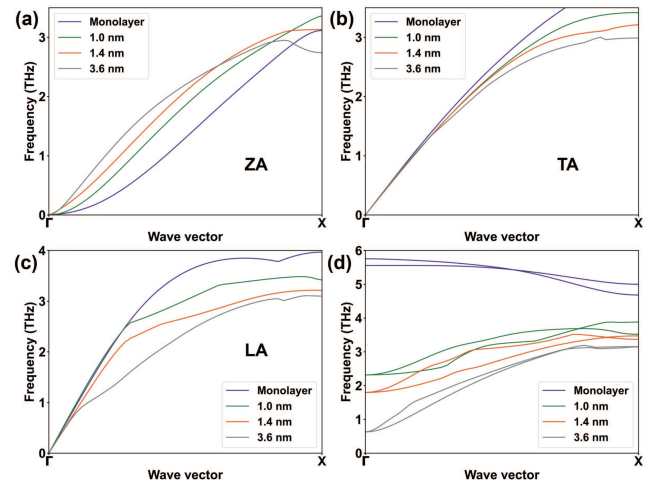


FIG. 5. Renormalized phonon dispersion relations of the (a) ZA, (b) TA, (c) LA, and (d) the lowest optical phonon branches along the Γ -X path of SrTiO_3 thin films with different thicknesses at 300 K.

branches along the Γ -X path are displayed. Full range phonon dispersions are shown in Fig. S10). No imaginary frequency phonon modes are found, which demonstrates the lattice stability of SrTiO_3 thin films at 300 K. Moreover, the ZA phonon branches of SrTiO_3 thin films exhibit clear thickness dependence, and along the Γ -X path, the ZA phonons largely harden as thickness increases. Such a hardening effect with thickness is also observed in Si thin films [22, 25]. The phonon dispersion near the Γ point changes from a quadratic curve to one that includes a linear term. Therefore, the hardening effect can increase the phonon group velocity and influence the scattering processes of low-frequency acoustic phonons. In addition, the low-frequency optical phonon branches at the Γ point gradually approach zero frequency as thickness increases. With the NEP and HNEMD simulations, we calculated the in-plane thermal conductivities of SrTiO_3 thin films with thickness from the monolayer limit to 10 nm at 300 K, as plotted in Fig. 6(a) together with the bulk value calculated from the HNEMD simulations. In Fig. 6(b), we show the thickness-dependent normalized in-plane thermal conductivity of van der Waals materials (graphene, MoS_2 , and their multilayer counterparts) and covalent Si and GaN with smooth surfaces. The thermal conductivities of graphene and monolayer MoS_2 are much higher than their bulk values, and the in-plane thermal conductivity of van der Waals materials rapidly decreases towards their bulk values as thickness increases. For covalent solids such as Si and GaN, the in-plane thermal conductivities of thin films with smooth surfaces are all lower than their bulk values, and the in-plane thermal conductivity tends to increase and approach their bulk values as thickness increases. However, the thickness-dependent in-plane thermal conductivity of SrTiO_3 thin films is unique: the thermal conductivity of the mono-

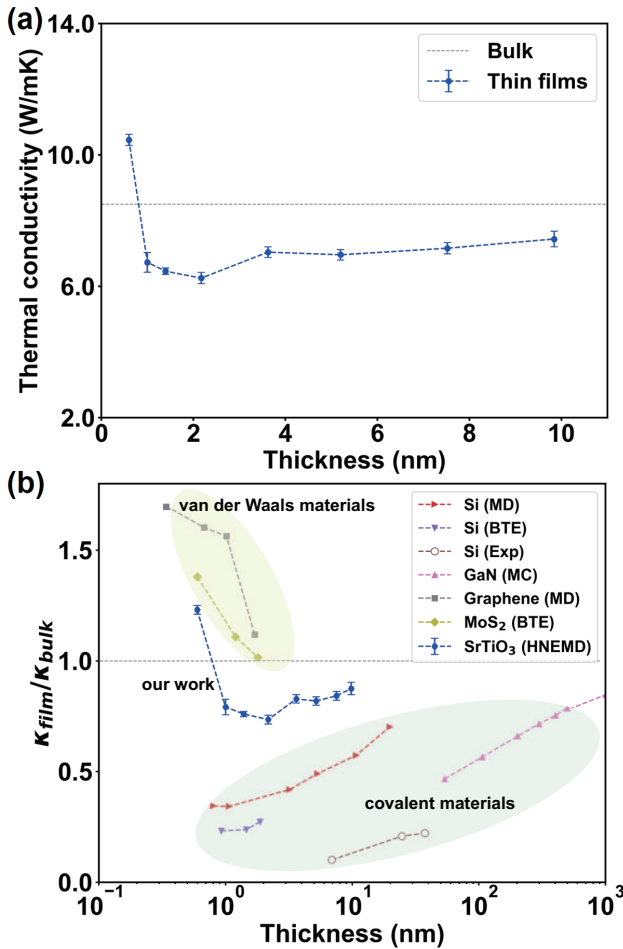


FIG. 6. (a) Thermal conductivity of SrTiO_3 thin films with different thicknesses at 300 K calculated from the HNEMD simulations. (b) Normalized thickness-dependent in-plane thermal conductivity ($\kappa_{film}/\kappa_{bulk}$) of different thin films including Si (MD[25], Exp[25], and BTE[22]), GaN [54], graphene [55], and MoS_2 [48]. Exp stands for experimental data, and MC represents Monte Carlo simulation.

layer is higher than that of bulk SrTiO_3 , while other SrTiO_3 thin films have slightly lower thermal conductivities than the bulk value. As the thickness increases from the monolayer limit to 1.0 nm, the thermal conductivity abruptly decreases from 10.5 to 6.7 W/mK (In the BTE method, the calculated thermal conductivity is reduced from 13.9 to 7.7 W/mK.). The minimal thermal conductivity is achieved at the thickness of 2.2 nm, and then the thermal conductivity slowly increases to the bulk value. With the increasing thickness of thin films, the hardening effect of the ZA phonon branch and the emergence of low-frequency optical phonon branches enlarge the possible phonon scattering channels, enhancing the phonon scattering strength of the dominant low-frequency phonons and lowering thermal conductivity. In Fig. 4, it is obvious that the contribution to the in-plane thermal conductivity is much reduced for the SrTiO_3 thin film with 1.0 nm thickness compared to the monolayer.

As thickness keeps increasing, the low-frequency optical phonon branches at the Γ point have little room to decrease. The rise of phonon group velocity resulting from ZA phonon hardening becomes dominant, and thermal conductivity gradually approaches the bulk value. In Fig. S11(a), we also plot the potential energy surfaces (PESs) with respect to the atomic displacements along the phonon eigenvector directions at 300 K corresponding to the lowest phonon modes at M point for SrTiO_3 thin films with different thicknesses. For monolayer and 1.0-nm-thick SrTiO_3 thin film, the PESs are single well; while for thicker films, the PESs become double well. By examining the atomic vibrational modes of different phonons at M point, we find that the rotational vibration modes along a (or b) axis of the $[\text{TiO}_6]$ octahedra (see Fig. S11(b)) appear when the thickness is larger than 1.0 nm, which is consistent with the variation of the PES from single well to double well. Analysis of the PES and atomic vibrational modes provides further insight into the highest thermal conductivity of monolayer SrTiO_3 among these thin films.

V. CONCLUSION

In summary, we have investigated the in-plane phonon transport in monolayer SrTiO_3 and ultrathin SrTiO_3 films with different thicknesses up to 10 nm by constructing an accurate machine-learning NEP. The renormalized phonon dispersion of monolayer SrTiO_3 is insensitive to temperature change, distinguished from its bulk counterpart. Using both the BTE method and HNEMD simulations, the thermal conductivity of monolayer SrTiO_3 is demonstrated to be higher than that of the bulk due to the changed ZA phonon branches and much-enhanced heat conduction of low-frequency phonon modes in monolayer SrTiO_3 . The thickness-dependent in-plane thermal conductivity of SrTiO_3 thin films is also extracted from the HNEMD simulations. As the thickness increases from the monolayer limit to 10 nm, thermal conductivity first decreases abruptly and then increases slowly to approach the bulk value. The thickness-induced low-frequency ZA phonon branch hardening and optical phonon branch softening largely affect the acoustic phonon scattering channels and phonon group velocity, which account for the observed trend of thermal conductivity transitions. This work uncovers the transition of thermal conductivity of SrTiO_3 thin films from the monolayer limit to 10 nm with first-principles accuracy and deepens the understanding of phonon transport in oxide perovskite thin films.

ACKNOWLEDGMENTS

The authors are grateful for the research computing facilities offered by ITS, HKU.

[1] Y.-Y. Sun, M. L. Agiorgousis, P. Zhang, and S. Zhang, Chalcogenide perovskites for photovoltaics, *Nano letters* **15**, 581 (2015).

[2] G. Grancini and M. K. Nazeeruddin, Dimensional tailoring of hybrid perovskites for photovoltaics, *Nature Reviews Materials* **4**, 4 (2019).

[3] H.-Y. Zhang, X.-J. Song, H. Cheng, Y.-L. Zeng, Y. Zhang, P.-F. Li, W.-Q. Liao, and R.-G. Xiong, A three-dimensional lead halide perovskite-related ferroelectric, *Journal of the American Chemical Society* **142**, 4604 (2020).

[4] Y. Zhou, J. Wang, D. Luo, D. Hu, Y. Min, and Q. Xue, Recent progress of halide perovskites for thermoelectric application, *Nano Energy* **94**, 106949 (2022).

[5] Q. Wang, Z. Zeng, P. Zhao, C. Chen, N. Ouyang, J. Mao, and Y. Chen, B-Site Columnar-Ordered Halide Double Perovskites: Breaking Octahedra Motions Induces Strong Lattice Anharmonicity and Thermal Anisotropy, *Chemistry of Materials* **35**, 1633 (2023).

[6] A. G. Ricciardulli, S. Yang, J. H. Smet, and M. Saliba, Emerging perovskite monolayers, *Nature Materials* **20**, 1325 (2021).

[7] S. G. Motti, T. Crothers, R. Yang, Y. Cao, R. Li, M. B. Johnston, J. Wang, and L. M. Herz, Heterogeneous photon recycling and charge diffusion enhance charge transport in quasi-2D lead-halide perovskite films, *Nano letters* **19**, 3953 (2019).

[8] F. Xia, H. Wang, D. Xiao, M. Dubey, and A. Ramanathan, Two-dimensional material nanophotonics, *Nature Photonics* **8**, 899 (2014).

[9] X. Qi, Y. Zhang, Q. Ou, S. T. Ha, C.-W. Qiu, H. Zhang, Y.-B. Cheng, Q. Xiong, and Q. Bao, Photonics and optoelectronics of 2D metal-halide perovskites, *Small* **14**, 1800682 (2018).

[10] J.-K. Huang, Y. Wan, J. Shi, J. Zhang, Z. Wang, W. Wang, N. Yang, Y. Liu, C.-H. Lin, X. Guan, *et al.*, High- κ perovskite membranes as insulators for two-dimensional transistors, *Nature* **605**, 262 (2022).

[11] D. Ji, S. Cai, T. R. Paudel, H. Sun, C. Zhang, L. Han, Y. Wei, Y. Zang, M. Gu, Y. Zhang, *et al.*, Freestanding crystalline oxide perovskites down to the monolayer limit, *Nature* **570**, 87 (2019).

[12] Z. Zhang and R. M. Wentzcovitch, Ab initio lattice thermal conductivity of MgSiO_3 across the perovskite-postperovskite phase transition, *Phys. Rev. B* **103**, 144103 (2021).

[13] Q. Wang, Z. Zeng, and Y. Chen, Revisiting phonon transport in perovskite SrTiO_3 : Anharmonic phonon renormalization and four-phonon scattering, *Physical Review B* **104**, 235205 (2021).

[14] L. Feng, T. Shiga, and J. Shiomi, Phonon transport in perovskite SrTiO_3 from first principles, *Applied Physics Express* **8**, 071501 (2015).

[15] Z. Zhang, K. Yuan, J. Zhu, X. Fan, J. Zhou, and D. Tang, Thermal conductivity of SrTiO_3 under high-pressure, *Applied Physics Letters* **120**, 262201 (2022).

[16] O. Hellman, P. Steneteg, I. A. Abrikosov, and S. I. Simak, Temperature dependent effective potential method for accurate free energy calculations of solids, *Physical Review B* **87**, 104111 (2013).

[17] O. Hellman, I. Abrikosov, and S. Simak, Lattice dynamics of anharmonic solids from first principles, *Physical Review B* **84**, 180301 (2011).

[18] T. Tadano and S. Tsuneyuki, Self-consistent phonon calculations of lattice dynamical properties in cubic SrTiO_3 with first-principles anharmonic force constants, *Physical Review B* **92**, 054301 (2015).

[19] X. Li, B. Fauqué, Z. Zhu, and K. Behnia, Phonon thermal hall effect in strontium titanate, *Physical review letters* **124**, 105901 (2020).

[20] J.-J. Zhou, O. Hellman, and M. Bernardi, Electron-phonon scattering in the presence of soft modes and electron mobility in SrTiO_3 perovskite from first principles, *Physical review letters* **121**, 226603 (2018).

[21] V. Martelli, J. L. Jiménez, M. Continentino, E. Baggio-Saitovitch, and K. Behnia, Thermal transport and phonon hydrodynamics in strontium titanate, *Physical review letters* **120**, 125901 (2018).

[22] Q. Wang, R. Guo, C. Chi, K. Zhang, and B. Huang, Direct first-principle-based study of mode-wise in-plane phonon transport in ultrathin silicon films, *International Journal of Heat and Mass Transfer* **143**, 118507 (2019).

[23] B. Fu, K. D. Parrish, H.-Y. Kim, G. Tang, A. J. McGaughey, *et al.*, Phonon confinement and transport in ultrathin films, *Physical Review B* **101**, 045417 (2020).

[24] M. Morita and T. Shiga, Surface phonons limit heat conduction in thin films, *Physical Review B* **103**, 195418 (2021).

[25] S. Neogi, J. S. Reparaz, L. F. C. Pereira, B. Graczykowski, M. R. Wagner, M. Sledzinska, A. Shchepetov, M. Prunnila, J. Ahopelto, C. M. Sotomayor-Torres, *et al.*, Tuning thermal transport in ultrathin silicon membranes by surface nanoscale engineering, *ACS nano* **9**, 3820 (2015).

[26] E. Chávez-Ángel, J. S. Reparaz, J. Gomis-Bresco, M. R. Wagner, J. Cuffe, B. Graczykowski, A. Shchepetov, H. Jiang, M. Prunnila, J. Ahopelto, *et al.*, Reduction of the thermal conductivity in free-standing silicon nanomembranes investigated by non-invasive Raman thermometry, *APL Materials* **2**, 012113 (2014).

[27] Y. Kuang, L. Lindsay, and B. Huang, Unusual enhancement in intrinsic thermal conductivity of multilayer graphene by tensile strains, *Nano letters* **15**, 6121 (2015).

[28] X. Gu, Y. Wei, X. Yin, B. Li, and R. Yang, Colloquium: Phononic thermal properties of two-dimensional materials, *Reviews of Modern Physics* **90**, 041002 (2018).

[29] P. Korotaev, I. Novoselov, A. Yanilkin, and A. Shapeev, Accessing thermal conductivity of complex compounds by machine learning interatomic potentials, *Physical Review B* **100**, 144308 (2019).

[30] H. Dong, C. Cao, P. Ying, Z. Fan, P. Qian, and Y. Su, Anisotropic and high thermal conductivity in monolayer quasi-hexagonal fullerene: A comparative study against bulk phase fullerene, *International Journal of Heat and Mass Transfer* **206**, 123943 (2023).

[31] J. Tang, G. Li, Q. Wang, J. Zheng, L. Cheng, and R. Guo, Competition between phonon-vacancy and four-phonon scattering in cubic boron arsenide by machine learning interatomic potential, *Physical Review Materials* **7**, 044601 (2023).

[32] C. Mangold, S. Chen, G. Barbalinardo, J. Behler, P. Pochet, K. Termentzidis, Y. Han, L. Chaput, D. Lacroix, and D. Donadio, Transferability of neural network potentials for varying stoichiometry: Phonons and thermal conductivity of Mn_xGe_y compounds, *Journal of Applied Physics* **127**, 244901 (2020).

[33] X. Qian and R. Yang, Machine learning for predicting thermal transport properties of solids, *Materials Science and Engineering: R: Reports* **146**, 100642 (2021).

[34] Y. Luo, M. Li, H. Yuan, H. Liu, and Y. Fang, Predicting lattice thermal conductivity via machine learning: a mini review, *npj Computational Materials* **9**, 4 (2023).

[35] Z. Fan, Z. Zeng, C. Zhang, Y. Wang, K. Song, H. Dong, Y. Chen, and T. Ala-Nissila, Neuroevolution machine learning potentials: Combining high accuracy and low cost in atomistic simulations and application to heat transport, *Physical Review B* **104**, 104309 (2021).

[36] Z. Fan, Y. Wang, P. Ying, K. Song, J. Wang, Y. Wang, Z. Zeng, K. Xu, E. Lindgren, J. M. Rahm, *et al.*, GPUMD: A package for constructing accurate machine-learned potentials and performing highly efficient atomistic simulations, *The Journal of Chemical Physics* **157**, 114801 (2022).

[37] D. J. Evans, Homogeneous NEMD algorithm for thermal conductivity—Application of non-canonical linear response theory, *Physics Letters A* **91**, 457 (1982).

[38] P. E. Blöchl, Projector augmented-wave method, *Physical review B* **50**, 17953 (1994).

[39] J. P. Perdew, A. Ruzsinszky, G. I. Csonka, O. A. Vydrov, G. E. Scuseria, L. A. Constantin, X. Zhou, and K. Burke, Restoring the Density-Gradient Expansion for Exchange in Solids and Surfaces, *Phys. Rev. Lett.* **100**, 136406 (2008).

[40] P. Korotaev, I. Novoselov, A. Yanilkin, and A. Shapeev, Accessing thermal conductivity of complex compounds by machine learning interatomic potentials, *Physical review B* **100**, 144308 (2019).

[41] K. Gubaev, E. V. Podryabinkin, G. L. Hart, and A. V. Shapeev, Accelerating high-throughput searches for new alloys with active learning of interatomic potentials, *Computational Materials Science* **156**, 148 (2019).

[42] G. Kresse and J. Furthmüller, Efficient iterative schemes for ab initio total-energy calculations using a plane-wave basis set, *Physical review B* **54**, 11169 (1996).

[43] S. Plimpton, Fast Parallel Algorithms for Short-Range Molecular Dynamics, *Journal of Computational Physics* **117**, 1 (1995).

[44] A. Togo and I. Tanaka, First principles phonon calculations in materials science, *Scripta Materialia* **108**, 1 (2015).

[45] W. Li, J. Carrete, N. A. Katcho, and N. Mingo, Sheng-BTE: A solver of the Boltzmann transport equation for phonons, *Computer Physics Communications* **185**, 1747 (2014).

[46] Z. Han, X. Yang, W. Li, T. Feng, and X. Ruan, Four-Phonon: An extension module to ShengBTE for computing four-phonon scattering rates and thermal conductivity, *Computer Physics Communications* **270**, 108179 (2022).

[47] See Supplemental Material at [URL will be inserted by publisher] for the validation of the NEP, details of the BTE calculations, details of the HNEMD simulations, and potential energy surface, which includes Refs. [37,58,59].

[48] X. Gu, B. Li, and R. Yang, Layer thickness-dependent phonon properties and thermal conductivity of MoS_2 , *Journal of Applied Physics* **119**, 085106 (2016).

[49] N. Bonini, J. Garg, and N. Marzari, Acoustic phonon lifetimes and thermal transport in free-standing and strained graphene, *Nano letters* **12**, 2673 (2012).

[50] J. Carrete, W. Li, L. Lindsay, D. A. Broido, L. J. Gallego, and N. Mingo, Physically founded phonon dispersions of few-layer materials and the case of borophene, *Materials Research Letters* **4**, 204 (2016).

[51] S. R. Popuri, A. Scott, R. Downie, M. Hall, E. Suard, R. Decourt, M. Pollet, and J.-W. Bos, Glass-like thermal conductivity in $SrTiO_3$ thermoelectrics induced by A-site vacancies, *Rsc Advances* **4**, 33720 (2014).

[52] Q. Wang, R. Guo, B. Huang, and Y. Chen, Unusual width dependence of lattice thermal conductivity in ultranarrow armchair graphene nanoribbons with unpassivated edges, *The Journal of Physical Chemistry C* **125**, 6034 (2021).

[53] G. Fugallo, A. Cepellotti, L. Paulatto, M. Lazzeri, N. Marzari, and F. Mauri, Thermal conductivity of graphene and graphite: collective excitations and mean free paths, *Nano letters* **14**, 6109 (2014).

[54] R. Wu, R. Hu, and X. Luo, First-principle-based full-dispersion Monte Carlo simulation of the anisotropic phonon transport in the wurtzite GaN thin film, *Journal of Applied Physics* **119**, 145706 (2016).

[55] Z. Wei, Z. Ni, K. Bi, M. Chen, and Y. Chen, In-plane lattice thermal conductivities of multilayer graphene films, *Carbon* **49**, 2653 (2011).

[56] Z. Fan, H. Dong, A. Harju, and T. Ala-Nissila, Homogeneous nonequilibrium molecular dynamics method for heat transport and spectral decomposition with many-body potentials, *Physical Review B* **99**, 064308 (2019).

[57] Y. Wang, N. Xu, D. Li, and J. Zhu, Thermal properties of two dimensional layered materials, *Advanced Functional Materials* **27**, 1604134 (2017).

[58] G. Bussi and M. Parrinello, Accurate sampling using langevin dynamics, *Physical Review E* **75**, 056707 (2007).

[59] F. Eriksson, E. Fransson, and P. Erhart, The Hiphive Package for the extraction of high-order force constants by machine learning, *Advanced Theory and Simulations* **2**, 1800184 (2019).